Erschienen in: Small ; 13 (2017), 9. - 1602702
https://dx.doi.org/10.1002/smll.201602702

Structure and Magnetic Property Control of Copper Hydroxide Acetate by Non-Classical Crystallization

*RuiQi Song, Theodora Krasia-Christoforou, Christian Debus, and Helmut Cölfen**

Copper hydroxide acetate (CHA), one layered hydroxide compound with tunable magnetism, attracts great interest because of its potential applications in memory devices. However, ferromagnetism for CHA is only demonstrated by means of GPa pressure. Herein, a new method is reported, involving the combination of different crystallization pathways to control crystallization of amorphous CHA toward the formation of CHA/polymer composites with tunable magnetic properties and even a tunability that can be tested at room temperature. By using poly[(ethylene glycol)$_6$ methyl ether methacrylate]-block-poly[2-(acetoacetoxy) ethyl methacrylate] (PEGMA-b-PAEMA) diblock copolymers as additives in combination with a post-treatment process by ultracentrifugation, it is demonstrated that CHA and PEGMA-b-PAEMA form composites exhibiting different magnetic properties, depending on CHA in-plane nanostructures. Analytical characterization reveals that crystallization of CHA is induced by ultracentrifugation, during which CHA nanostructures can be well controlled by changing the degrees of polymerization of the PEGMA and PAEMA blocks and their block length ratios. These findings not only present the first example of using crystallization from polymer stabilized amorphous precursors toward the generation of magnetic nanomaterials with tunable magnetism but also pave the way for the future design of functional composite materials.

1. Introduction

Layered hydroxide compounds (LHCs) raised steadily increasing scientific interest in the last 20 years because of the possibility to functionalize these materials by intercalating organic molecules that can introduce new physical properties.[1] Copper hydroxide acetate (CHA) (Figure S1, Supporting Information) is a well-known LHC, exhibiting metamagnetic properties.[1,2] Each layer of CHA contains a planar triangular array of copper atoms bridged by μ^3—OH or μ^3—O of acetate anions. The coexistence of interlayer antiferromagnetic and in-plane ferromagnetic interactions provides the possibility of tuning magnetism.[3–7] Based on previous studies, CHA and its analogues often show antiferromagnetic behavior.[1,6] So far, strategies reported for inducing the antiferromagnetism (AF)-ferromagnetism (F) transition for CHA have been limited to applying GPa pressure[2] or changing the internal pressure by means of chemical substitutions of insertion species.[4,8–13]

Tracking advances in other materials with AF-F effects helps to generate new strategies. CHA and intermetallic compounds, both of which are metamagnetic materials with layered structures, present a common situation, where the magnetic properties of these compounds may arise from

Dr. R. Q. Song, Prof. H. Cölfen[+]
Max-Planck-Institute of Colloids and Interfaces
Am Mühlenberg
14424 Potsdam, Germany
E-mail: helmut.coelfen@uni-konstanz.de
Dr. T. Krasia-Christoforou
Department of Mechanical and Manufacturing Engineering
University of Cyprus
1678 Nicosia, Cyprus
C. Debus
Physical Chemistry
University of Konstanz
Universitätsstr. 10, 78464 Konstanz, Germany
[+]Present address: Physical Chemistry, University of Konstanz, Universitätsstr. 10, 78464 Konstanz, Germany

new types of spin coupling that has the ability to generate magnetic transitions. Studies on temperature or field-induced AF-F phase transition of intermetallic compounds suggest that the magnitude of the interlayer interaction strongly depends on the 3d transition metal atom distance.[14,15] We hypothesized that an AF-F transition could arise from crystallization toward the formation of CHA crystals with particle-based structures.

Testing our hypothesis is difficult. Several important obstacles need to be overcome to achieve a desired control over crystallization. First, the synthesis of amorphous CHA materials, especially when using nanoparticles as building blocks, has remained unknown. In contrast, crystallization kinetics places an energetic restriction on the formation of CHA amorphous materials since the precipitation of CHA crystallized compounds is extremely fast.[3,4,8–13] Second, the transformation of amorphous CHA to crystallized products excluding any CHA oxidation effect is required. Thus, the synthesis of nanoparticle-based CHA compounds remains to be demonstrated, though CHA materials have been known for a long time.

To validate our hypothesis, we relied on using amphiphilic block copolymers (ABCs) as additives in combination with ultracentrifugation to exert control over crystallization of carbonate-incorporated copper hydroxide acetate (CICHA). Our goal is to combine different crystallization pathways that can be utilized to organize amorphous nanoparticles into nanosized precursors and transform the amorphous precursors to crystallized materials with nanoparticle-based structures. The use of ABCs is based on the effective role of polymeric additives in stabilizing amorphous precursors, forming micelles that can be used as reactors for crystallization to occur in confinement.[16] Crystallinity-dependent spin crossover properties were found for iron complex nanoparticles formed in polystyrene-*b*-poly(4-vinylpridididine) ABC micelles.[17] The reason for our selection of three ABCs that belong to one specific family will be provided later. Our consideration of applying ultracentrifugation is to induce crystallization at room temperature without destroying the amorphous precursors that contain ABCs in order to expand the opportunity to make use of ABCs when designing control strategies for crystallization processes. No studies have so far been conducted on magnetic property control via combined crystallization pathways enabling the transformation of polymer stabilized amorphous precursors to crystallized products at room temperature. Although the formation of transitional amorphous precursor phases is involved in the early stage of sol-gel processing of $BiFeO_3$ (BFO) materials with AF-F transition, these sol-gel processes are typically polycondensation reactions followed by annealing to promote crystallization, which results in the formation of non-uniform micro-sized particle agglomerates that are different from our intended product morphology. More importantly, the occurrence of an AF-F transition for sol-gel method derived BFO materials was demonstrated based on rare earth doping induced lattice distortion[18] or BFO crystal phase transition that can be caused by substrate induced strain effects.[19] These mechanisms make our study different from prior studies on sol-gel processing for magnetic transition. Similarly, no previous studies have yet been conducted on using centrifugation to induce crystallization of magnetic materials. A few existing studies on using centrifugation have shown the important effect of centrifugation on bringing particles into close proximity.[20–23] In comparison with these studies, crystallization herein is based on using amorphous precursors composed of nanoparticles, ABC additives,[23] and using centrifugation to induce parallel arrangements or fusion of nanoparticles, which would induce synergistic effects on changing magnetic properties.

2. Results and Discussion

2.1. Strategy Overview

In order to exert control over structure and magnetic behavior of CICHA, we used poly[(ethylene glycol)$_6$ methyl ether methacrylate]-*block*-poly[2-(acetoacetoxy) ethyl methacrylate] (PEGMA-*b*-PAEMA) ABCs (Table S1, Supporting Information) as additives.[24] Due to the hydrophobic PAEMA and the hydrophilic PEGMA blocks, micelles are generated in water that can provide access to crystallization in confinement. The PEGMA and PAEMA block lengths provide a means for controlling the micellar structure and composition. Another reason for choosing PEGMA-*b*-PAEMA as additives was to use the β-ketoester segments and the PEG chains existing in PAEMA and PEGMA blocks, respectively. While the β-ketoester segments can coordinate with copper cations,[25] hydrogen bonding occurring between copper hydroxyl units and PEG can afford an additional advantage beyond micellization in exerting control over product structures. These advantages not previously reported include providing templates for confinement, stabilization of amorphous nanoparticles, inhibiting crystallization, and self-assembly of amorphous nanoparticle/ABC composites.

A scheme of the experimental process is provided in **Figure 1**. Three steps can be distinguished in the case of polymer-controlled crystallization: The first step involves the micellization of PEGMA-*b*-PAEMA (Step 1). The second step allows the formation of CICHA nanoparticles and the self-assembly of CICHA nanoparticles and PEGMA-*b*-PAEMA additives into amorphous nanobelts (Step 2) upon diffusion of carbon dioxide and ammonia into an aqueous solution of copper acetate and PEGMA-*b*-PAEMA. The third step consists of ultracentrifugation-induced crystallization of CICHA (Step 3). As demonstrated below, in the absence of PEGMA-*b*-PAEMA, CICHA amorphous nanoparticles fuse into crystalline nanobelts forming lamellar structures. When the PEGMA block length is shorter (PEGMA$_{97}$-*b*-PAEMA$_{18}$) nanoparticles also fuse together, resulting in the formation of a lamellar structure with condensed inorganic sheets (c1). In the case of the PEGMA$_{97}$-*b*-PAEMA$_{46}$, a similar situation is observed due to the presence of a larger amount of PAEMA blocks that favorably coordinate copper ions. Upon increasing the DP of the PEGMA block, from 97 to 292, while retaining a lower ratio of PEGMA to PAEMA (97:12), the generation of larger micelles with a

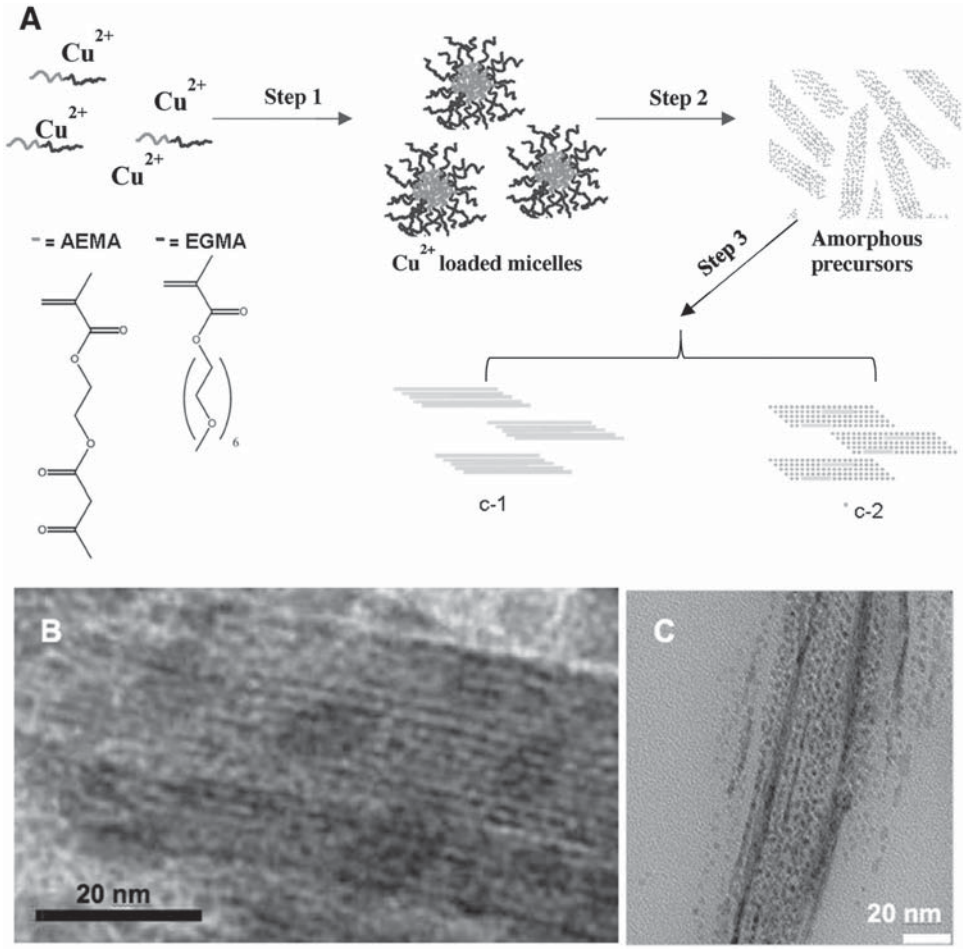

Figure 1. A) Schematic illustration of the process toward structure control over CICHA composite products by an ultracentrifugation induced crystallization of amorphous CICHA that are stabilized by PEGMA$_x$-*b*-PAEMA$_y$ polymeric additives. B,C) TEM image of composite materials showing a switch of structural features of CICHA from condensed lamellae (CICHA/PEGMA$_{97}$-*b*-PAEMA$_{46}$ and CICHA/PEGMA$_{97}$-*b*-PAEMA$_{18}$) to ordered nanoparticles (CICHA/PEGMA$_{292}$-*b*-PAEMA$_{36}$).

much thicker shell enables a parallel arrangement of nanoparticles as a result of the inhibited fusion between individual particles (c2). Once identified, the difference in structures of CICHA will provide an opportunity to manipulate the magnetic properties of CICHA/polymer composites.

2.2. Synthesis and Characterization of the Control Sample

Nanosheets with micrometer-sized non-uniform length and width of 100–200 nm (Figure S2B,C-a, Supporting Information) were obtained when no polymeric additive was added. It is difficult to measure the thickness of these nanosheets because of their dense packing fashion. A lamellar structure, as evidenced by X-ray diffraction (XRD) (Figure S2A, Supporting Information), can be seen from the arrow-labeled areas of CICHA nanosheets (Figure S2C-c, Supporting Information). The XRD (Figure 4A) and selected area electron diffraction (SAED) patterns (inset of Figure S2C-d, Supporting Information), revealed the formation of a crystallized product. Interestingly, the incorporation of carbonate increases the d_{001} spacing from 0.93 nm for the pristine CHA[4] to 1.58 nm for the resulting CICHA. Fourier Transform Infrared Spectroscopy (FT-IR) identified the presence of carbonate, acetate, hydroxyl, methyl groups, and water (Figure S3, Table S2, Supporting Information). CICHA nanosheets with (001) planes parallel to the substrate surface were also characterized. As evidenced by transmission electron microscopy (TEM) images (Figure S2C-a,b, Supporting Information), tip areas comprised of randomly oriented nanoparticles were observed for some of these nanosheets. Estimation using the Scherrer equation gives the average crystallite size of 12 nm (Table S3, Supporting Information).

2.3. Copper-Incorporated Micellization of PEGMA-*b*-PAEMA

Atomic force microscopy (AFM) measurements allow for the direct comparison between PEGMA-*b*-PAEMA micelles and copper-incorporated analogues. **Figure 2** shows a typical AFM image for PEGMA$_{97}$-*b*-PAEMA$_{46}$ micelles (images A and B in Figure 2) with a uniform diameter around 40 nm (Figure S4A, Supporting Information) generated in aqueous solution. This value is comparable to the hydrodynamic diameter of 45 nm obtained by dynamic light scattering (DLS) (Table S1, Supporting Information). Copper ion-loaded PEGMA$_{97}$-*b*-PAEMA$_{46}$ micelles, which are formed in the

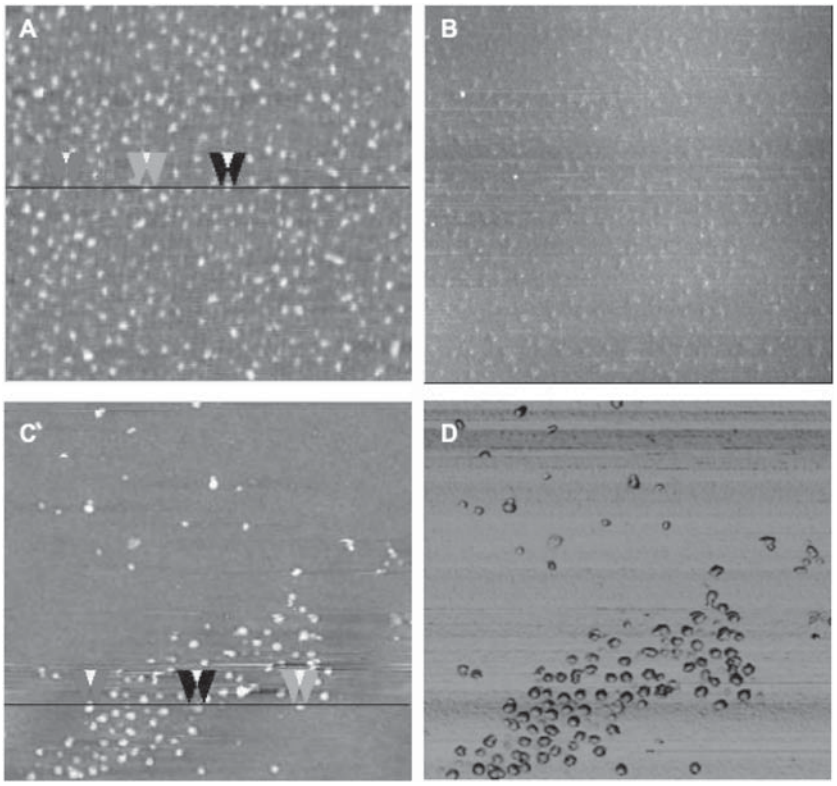

Figure 2. AFM images of micelles. $PEGMA_{97}$-*b*-$PAEMA_{46}$ micelles formed in water: A) height image and B) phase image. Micelles formed in copper acetate/$PEGMA_{97}$-*b*-$PAEMA_{46}$ aqueous solution: C) height image and D) phase image. Scan size: 1 × 1 µm (A,B); 1.3 × 1.3 µm (C,D). The height profiles in (A) and (C) are given in Figure S4 (Supporting Information).

aqueous copper acetate solution, are larger in size (images C and D in Figure 2) with a diameter of 45–47 nm (Figure S4B, Supporting Information). Moreover, AFM phase images reveal compositional differences between the two micelle types. The bi-phased topography of core–shell like structures with a typical layer thickness of about 8–9 nm (image D in Figure 2) indicates that the incorporation of copper ions in $PEGMA_{97}$-*b*-$PAEMA_{46}$ micelles takes place over the whole core–shell interface area of the micelles. In contrast, the copper-free micelles (image B in Figure 2 and images C and D in Figure S4, Supporting Information) show a monophase topography image.

The incorporation of copper ions into the polymer phase implies that the PEGMA-*b*-PAEMA micelles play a chemically specific role in the self-assembly of CICHA nanoparticles. Another significant difference can be found by comparing images B and D in Figure 2. Whereas the copper-free micelles are homogeneously dispersed, the copper ion-loaded micelles show a tendency to connect with each other, possibly due to hydrogen bonding between the copper hydroxyl units and the PEG chains of the PEGMA blocks. Formation of micellar aggregates with the size distribution centered at a few hundred nm was detected by DLS.

2.4. Formation and Assembly of Amorphous Nanoparticles

A TEM image of the precursor obtained in the presence of $PEGMA_{97}$-*b*-$PAEMA_{18}$ is shown in **Figure 3**A. Spherical structures with 30 nm in diameter composed of nanoparticles with an average diameter of 0.5–3 nm are formed from $PEGMA_{97}$-*b*-$PAEMA_{18}$ and Cu^{2+} upon gas diffusion over 12 h. In the PEGMA-*b*-PAEMA/Cu^{2+} system, the coordination of Cu^{2+} with the PAEMA blocks and their hydrophobicity play an important role in the formation of micelles. The addition of PEGMA-*b*-PAEMA results in the formation of copper ion-loaded micelles acting as nanoreactors for the uptake of other reactants and ensuing formation of amorphous CICHA nanoparticles under confinement.[26] The location and size of the nanoparticle clusters suggest that they were formed under the confinement of micelles.

Nanobelts with 50–300 nm in width, 10–20 nm in thickness, and up to a few micrometers in length (Figure 3B,E,F) were obtained in all cases using PEGMA-*b*-PAEMA as additives after 3 days. The formation of the amorphous CICHA was evidenced by the XRD patterns for these intermediates as shown in Figure S7 (Supporting Information) and the scattered SAED patterns for individual nanobelts provided in the inset of Figure 3C. The low angle peaks in the XRD profiles of these CICHA/PEGMA-*b*-PAEMA samples provide a direct evidence for determining the formation of bi-lamellar structures as labeled in Figure S7 (Supporting Information), while no high intensity peaks except a broad peak centered at 2θ of 21° can be identified for the XRD profiles. This result is remarkably different from the control sample for which the formation of a polycrystalline CICHA was detected after an equal period of reaction time, demonstrating that PEGMA-*b*-PAEMA works effectively as an inhibitor that can prevent amorphous CICHA materials from transforming into their crystallographic phases.

Moreover, the disassembly of CICHA/PEGMA-*b*-PAEMA nanobelts was realized by dispersing the nanobelts in 1-methyl-2 pyrrolidinone (MPD). The nanoparticle-based structural characteristics of nanobelts (Figure 3D and Figure S5C,D, Supporting Information) were evidenced by TEM images of individual nanobelts, suggesting a nanoparticle-based growth mechanism for CICHA/PEGMA-*b*-PAEMA nanobelts. The presence of the polymeric additive, the small grain size, and their amorphous nature make the observation of nanoparticles in this sample not comparable to the clear observation of nanoparticles in the tip areas of some nanosheets for the control sample, which are polycrystalline. The intermediate polarity of MPD enables the dissolution of both PEGMA and PAEMA blocks. Rather than a simple dissolution of organic regions,[27,28] the disassembly in the presented case involves breaking the connectivity between nanoparticles in 2D assemblies. In line with 2D nanoparticle assemblies being disintegrated (Figure S5, Supporting Information), large nanoparticles formed (B and D in Figure S5, Supporting Information) by Ostwald ripening. Some nanobelts even started

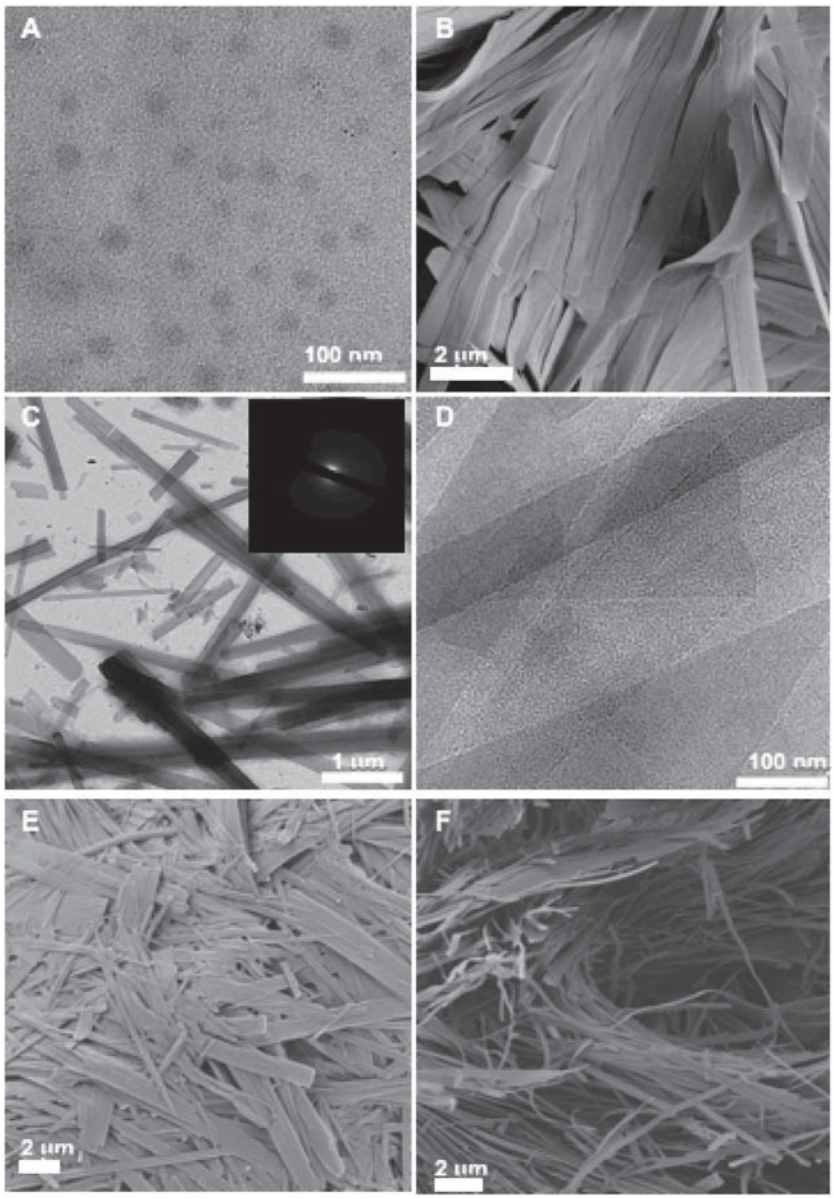

Figure 3. Electron microscopy images of colloidal precursors and 2D assemblies of amorphous CICHA nanoparticles: A) TEM image taken from the ultramicrotomed slices of the colloidal precursor obtained in the presence of $PEGMA_{97}$-*b*-$PAEMA_{18}$ upon gas diffusion after 12 h. B) SEM image and C,D) TEM images of CICHA nanoparticle belts obtained in the presence of $PEGMA_{97}$-*b*-$PAEMA_{18}$. SEM image of amorphous belts obtained in the presence of E) $PEGMA_{292}$-*b*-$PAEMA_{36}$ and F) $PEGMA_{97}$-*b*-$PAEMA_{46}$.

coiling due to frustration (A in Figure S5, Supporting Information). It is interesting to note that amorphous CICHA/PEGMA-*b*-PAEMA nanobelts can also be used as precursor to directly synthesize CuO mesocrystals in a hydrothermal reaction, which demonstrates the versatility of these block copolymers as additives for the generation of copper-based nanoparticle superstructures (Figure S6, Supporting Information).

2.5. Ultracentrifugation-Induced Crystallization

To obtain crystallized CICHA products from these amorphous nanobelts, we performed a post-synthesis treatment by ultracentrifugation. Ultracentrifugation-induced crystallization was confirmed by XRD (**Figure 4**A). The XRD profiles of all products obtained after ultracentrifugation (Figure 4A and the top profile in Figure S7, Supporting Information) show one identical feature with high intensity diffraction peaks in the high angle range, as compared to the XRD profiles of those before crystallization, which has a broad peak centered at 2θ of ≈21° without any other high intensity peaks at $2\theta > 20°$ (Figure S7 bottom, Supporting Information).

Crystallization is caused by sedimentation with subsequent aggregation of nanoparticles as a result of the pressure exerted on the aggregates.[20,21,29,30] Specifically, we would like to note that ultracentrifugation-generated pressure is over 2–3 orders of magnitude lower than the hydrostatic pressure that was used for reported AF-F or F-AF transitions.[2,31–34]

Crystallite sizes of CICHA in CICHA/PEGMA-PAEMA composite samples were also evaluated. As shown in Table S3 (Supporting Information), crystallization results in smaller crystallite sizes than the control sample. Regardless of the PEGMA:PAEMA block length ratio, the CICHA products possess sharp reflections in the range of low angles with two d_{001} distances as previously observed in other layered compounds.[35,36] The maximum peak at $2\theta = 5.5°$ varies slightly upon changing polymer composition. The incorporation of carbonate and inescapable water induces a significant enhancement of the basal spacing from 0.93 nm for CHA[3,4,10,13] to 1.59–1.61 nm for PEGMA-*b*-PAEMA-derived CICHA products. Presumably, carbonate ions and water molecules are bound to the OH groups of the main layers through hydrogen bonds and occupy the space between the layers. In addition, the rotation of interlayer water molecules and carbonate ions gave rise to a different orientation of these intercalates with a shorter basal spacing as observed from the peak at $2\theta = 7.5°$ (Figure 4A).

While ultra-long nanobelts were obtained after ultracentrifugation in the presence of $PEGMA_{97}$-*b*-$PAEMA_{18}$ or $PEGMA_{292}$-*b*-$PAEMA_{36}$ (Figure 4B,C, respectively), nanosheets with lengths up to several µm and widths of 50–300 nm were obtained by using $PEGMA_{97}$-*b*-$PAEMA_{46}$ (Figure 4D). Thermogravimetric analysis (TGA) (Figure S8, Supporting Information) shows weight loss with exothermic peaks at 300–550 °C indicating the presence of PEGMA-*b*-PAEMA because the PAEMA degradation process is highly exothermic.[37] These data demonstrate that the

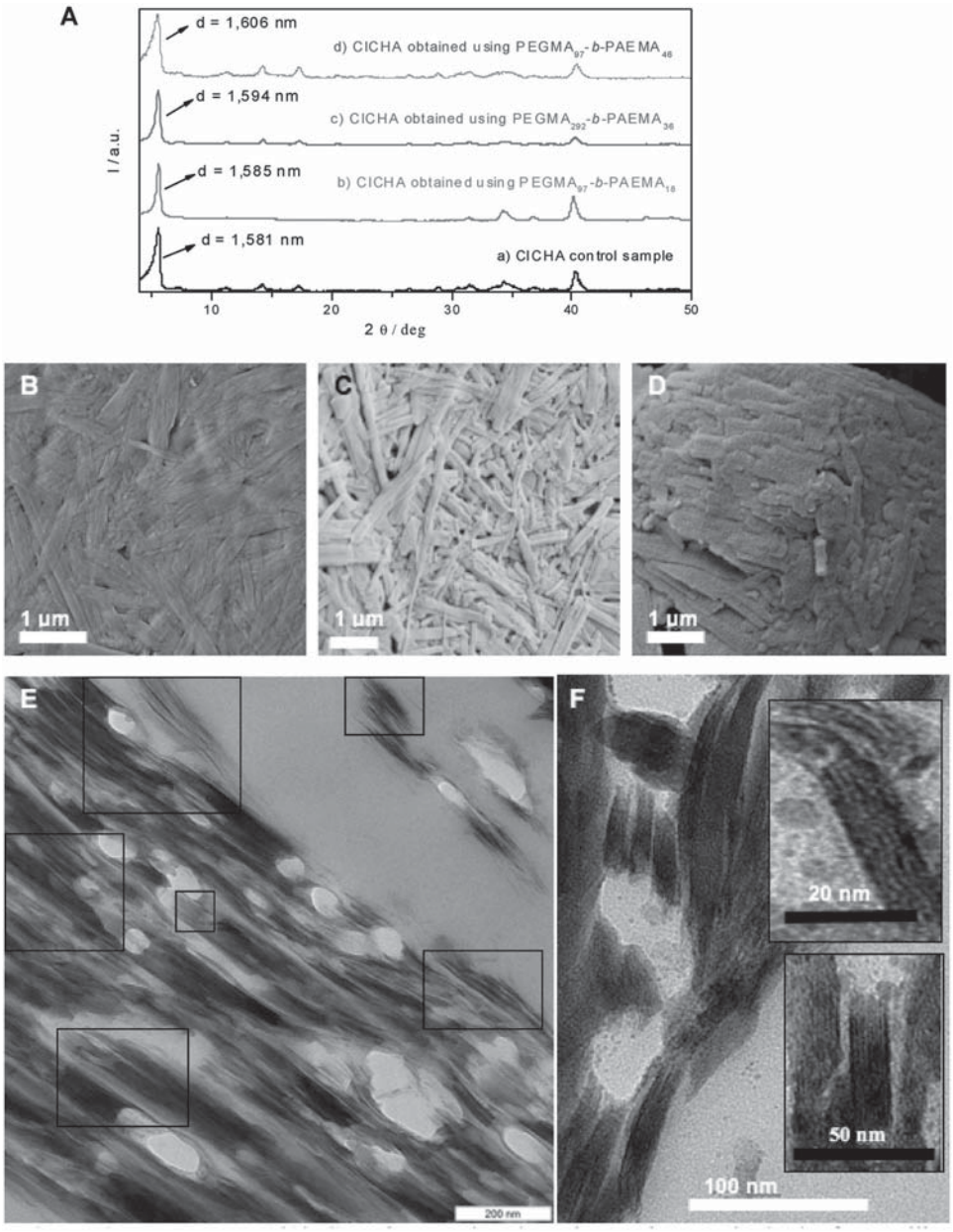

Figure 4. A) XRD patterns, B–D) SEM images, and E,F) TEM images of crystallized products. The images in (B) and (E) correspond to the CICHA sample obtained in the presence of $PEGMA_{292}$-*b*-$PAEMA_{36}$. Areas in black boxes are highlighted in (E) to reveal the visibility of a lamellar structure formed by nanoparticle ordering. The images in (C) and (F) correspond to the CICHA sample obtained in the presence of $PEGMA_{97}$-*b*-$PAEMA_{18}$. The images in (D) correspond to the CICHA sample obtained in the presence of $PEGMA_{97}$-*b*-$PAEMA_{46}$. The insets in (F) show the images taken at high magnification.

transformation from amorphous to crystallized CICHA nanobelts results in polymer inclusion. The polymer content is comparatively high (40%) when $PEGMA_{97}$-*b*-$PAEMA_{46}$ was used as an additive compared to 30%–35% for the two other block copolymers. The high loading level of PEGMA-*b*-PAEMA is probably related to the formation of flexible nanobelts and nanosheets that are superlong, as compared to the control sample comprised of rigid nanosheets with nonuniform lengths. The SAED patterns taken for CICHA/PEGMA-*b*-PAEMA are too weak to provide information that is useful to further characterize these samples due to the same reason. Granules adhering on the surface of CICHA/$PEGMA_{97}$-*b*-$PAEMA_{46}$ nanosheets were observed (Figure 4D). Phase separation is a possible reason for the formation of these granules that were observed to have poor contrast under TEM. FT-IR spectra of these CICHA products obtained in the presence of PEGMA-*b*-PAEMA show the C=O stretching vibration at 1729 cm^{-1} due to the presence of polymer residues (Figure S3, Supporting Information).

To gain further insights into the influence of PEGMA-*b*-PAEMA with varied block ratios, we used TEM to characterize the samples obtained after ultracentrifugation (Figure 4E,F). Parallel arrangements of nanoparticles consisting of primary nanoparticles, of ≈5 nm in size, were

observed when using PEGMA$_{292}$-*b*-PAEMA$_{36}$. Structure defects inducing peak broadening is the possible reason for the difference between grain size and crystallite size. The observation of individual nanoparticles and condensed nanosheets in the length of 100–200 nm in some areas supports the occurrence of non-classical crystallization, which is crystallization based on nanoparticle assembly.[38] Interestingly, the arrangement of the nanoparticles is parallel to the nanosheets, building up a highly ordered lamellar structure (Figures 1C and 4E). In comparison, nanobelts consisting of condensed lamellae were observed in the sample containing PEGMA$_{97}$-*b*-PAEMA$_{18}$ (Figures 1B and 4F) and PEGMA$_{97}$-*b*-PAEMA$_{46}$. In fact, both of these two types of structures of crystallized CICHA are different from the control sample. Consequently, these results indicate that the presented strategy grants an easy control over crystallization of CICHA and the formation of two new different types of CICHA nanostructures.

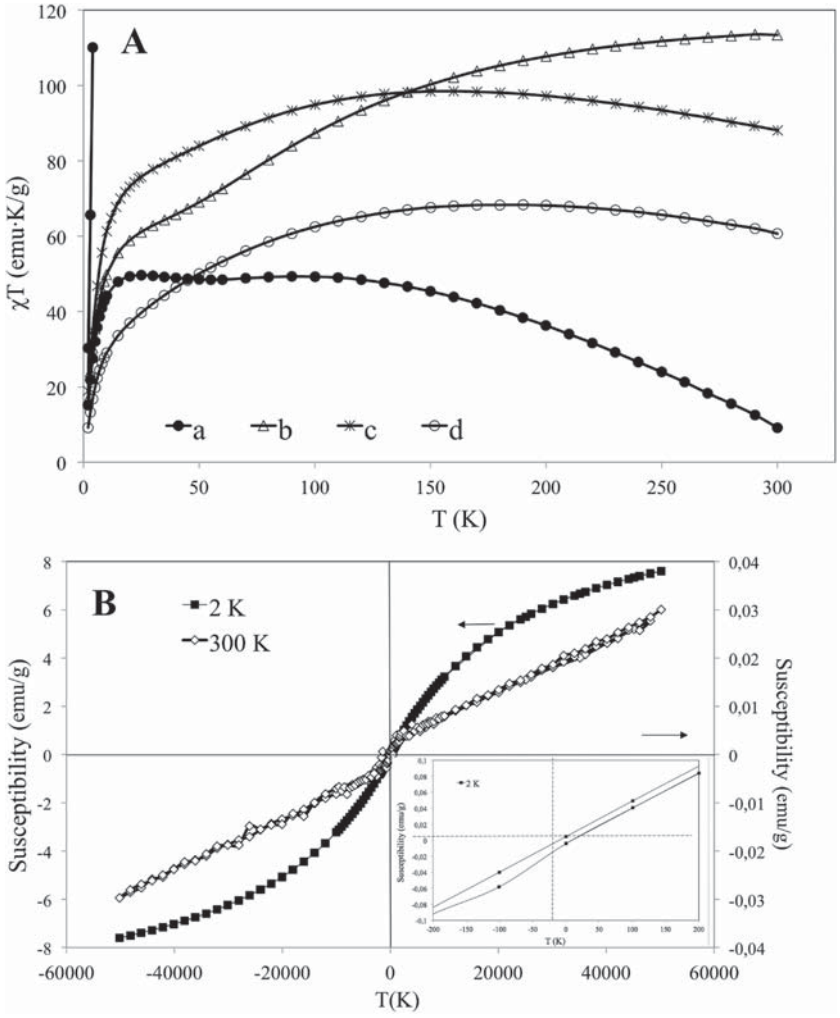

Figure 5. A) Temperature-dependence of χT measured at 5 T: CICHA products were obtained in the presence of PEGMA$_x$-*b*-PAEMA$_y$ with the *x*:*y* DP ratios of: a) 292:36, b) 97:18, and c) 97:46, and from the control experiment without using polymeric additives (d). B) The field dependence of magnetic susceptibility measured at 2 and 300 K for a CICHA product that was obtained in the presence of PEGMA$_x$-*b*-PAEMA$_y$ with the *x*:*y* DP ratios of 292:36 (scale of 300 K curve is on the right). The inset shows the low field profile at 2 K.

2.6. Characterization of Magnetic Properties of CICHA/PEGMA-*b*-PAEMA Nanobelts

The structural variation of these samples prompted us to investigate their magnetic behavior. **Figure 5**A depicts the temperature-dependent susceptibility of the investigated samples under an applied field of ±50 kOe. Upon cooling, the χT value for the product obtained with the addition of PEGMA$_{292}$-*b*-PAEMA$_{36}$ (plot a in Figure 5A) kept rising with a first peak observed at 90 K, followed by an almost constant χT value down to 50 K. Then a second ascension was obtained with a peak χT value at 25 K.

As shown in Figure 5A, the χT profile of the CICHA product obtained in the presence of PEGMA$_{97}$-*b*-PAEMA$_{18}$ decreases monotonically upon cooling. It exhibits a typical antiferromagnetic behavior over the whole temperature range (plot b in Figure 5A). The temperature dependence of χT for the CICHA product obtained using PEGMA$_{97}$-*b*-PAEMA$_{46}$ (plot c in Figure 5A) is very similar to that of the control product (plot d in Figure 5A). A slow increase of χT was observed for the product upon cooling with a broadened maximum at ≈175 K.

Figure 5B, and Figures S9 and S10 (Supporting Information) represent the magnetic performance of the samples obtained in magnetic fields of up to ±50 kOe at temperatures of 2 and 300 K. The most interesting results were noticed for the product obtained with the addition of PEGMA$_{292}$-*b*-PAEMA$_{36}$ (Figure 5B). Its magnetic susceptibility at both 2 and 300 K exhibited an S-shape dependence on the field with a visible hysteresis tendency at 2 K. The inset in Figure 5B shows a visible coercivity of 10 Oe at 2 K. The magnetization loops look characteristic for the combination of an S-shaped superparamagnetic contribution going into saturation and a linear contribution from the antiferromagnetic phase. What sets this sample apart from the other samples is the retention of the nanoparticle morphology. Superparamagnetism in antiferromagnetic nanoparticles has been reported for a variety of other systems[39–41] and is assumed to be caused by incomplete compensation of the surface spins, which constitute a major contribution at such small particle sizes.

This effect, albeit weaker, is also observed for the other CICHA products consisting of condensed bands, which were obtained using PEGMA$_{97}$-*b*-PAEMA$_{46}$ (Figure S10A, Supporting Information), PEGMA$_{97}$-*b*-PAEMA$_{18}$ (Figure S10B, Supporting Information), and in the absence of polymeric additives (Figure S10C, Supporting Information). Although these

samples no longer consist of individual nanoparticles, they still have two dimensions in the nm size range. While S shaped magnetization is also observed at 2 K, those magnetization loops show no visible hysteresis. Merely, a linear response was found for these products at 300 K.

The structures of CICHA in these composite products were significantly tuned by the crystallization strategy, which involves the combined[42] effects of several pathways including polymer-controlled crystallization, crystallization in confinement, non-classical crystallization, and parallel arrangements of nanoparticles induced by ultracentrifugation. Antiferromagnetic materials can be improved to a large extent when subjected to extra stimuli, such as drying,[37,43] laser heating,[44] and surface strain relief.[45] In our case, we assume that ultracentrifugation plays a similar role in synergy with the stabilization of polymeric additives. When $PEGMA_{97}$-*b*-$PAEMA_{18}$ was added, CICHA with highly condensed crystalline plates is formed after ultracentrifugation due to the fusion of nanoparticles with lower colloidal stability. However, lamellae consisting of parallel arrangements of nanoparticles are formed when $PEGMA_{292}$-*b*-$PAEMA_{36}$ was added. The PEGMA shell imparts sufficient colloidal stability to PAEMA-complexed CICHA nanoparticles and forms a polymeric coating. After drying, this provides mechanical integrity to maintain the extended parallel arrangements of nanoparticles through interdigitation of PEGMA chains. The distance between particles localized in one individual layer is a few nanometers in the CICHA product obtained in the presence of $PEGMA_{292}$-*b*-$PAEMA_{36}$ (the inset in Figure 4E), as observed by TEM. The structural variation possibly blocks exchange pathways between layers in a 3D long range. On the one hand, the structural variation leads to weaker interlayer exchange coupling due to changes both in nearest-neighbor and next-nearest-neighbor interactions between Cu 3d moments localized in adjacent Cu−Cu layers with the separation between copper atoms in neighboring particles.[15] On the other hand, the influence of nanoparticle-based structures on the in-plane ferromagnetic exchange energy is not negligible, as suggested by other studies discussing the dependence of AF-F transition on particle size.[42,46,47] A dipolar interaction-like interplay possibly becomes predominant because the number of weakly coupled uncompensated spins on CICHA nanoparticle surfaces may increase due to the frustrated in-plane exchange pathways caused by the nanoparticle-based structures. As a consequence, antiferromagnetism is depressed and ferromagnetism is enhanced.

The structure-dependent magnetic control investigated in this study differs from the known crossover that can be tailored by the bond angle mechanism. Previous experimental and theoretical findings on copper (II) hydroxo-based layered compounds suggested that the increase of the Cu−O−Cu bridge angle favors an antiferromagnetic coupling exchange of neighboring copper atoms.[2,48–50] The incorporation of carbonate separated the individual layers with *d*-spacings increasing to larger values than observed for CHA itself. Compared to the influence of particle-based crystal structures, variations in interlayer distance of the CICHA products obtained in the presence of PEGMA-*b*-PAEMA (Figure 4A) are not the primary cause for the improvement in ferromagnetism. To investigate the influence of ultracentrifugation on the geometry of the Cu−O−Cu exchange pathways, we compared the interlayer distance of the product obtained in the presence of $PEGMA_{97}$-*b*-$PAEMA_{46}$ before and after ultracentrifugation. Interestingly, a slight increase of the interplane distance in the *c*-direction was observed (Figure S7, Supporting Information), which indicates that the Cu−O−Cu angles decreased after crystallization. The result is consistent with the previous studies on $(Fe_{0.975}Ni_{0.025})_{50}Rh_{50}$ and MnBi, suggesting that AF-F transition occurs across the transformation from amorphous phase to crystallization.[51]

3. Conclusion

We have established a method for controlling the crystallization of CICHA toward the formation of CICHA/polymer composite materials with tunable magnetic properties. The method consists of three key steps establishing access to rational control over CICHA nanostructures. The first step is the formation and the incorporation of copper ions into ABC micelles. The second step involves the assembly of amorphous nanoparticles, which are confined, stabilized, and organized by ABCs, to form nanobelts, while the third step involves ultracentrifugation-induced crystallization. Depending on the lengths of the two block segments and the block length ratio of PEGMA-*b*-PAEMA additives, we can purposefully control CICHA nanostructures and magnetic properties of the resulting composite products. The results suggest that crystallization may provide a novel pathway to manipulate the physical properties of inorganic/polymer composites.

4. Experimental Section

Sample Preparation: $Cu(CH_3COO)_2{\bullet}H_2O$ and $(NH_4)_2CO_3$ were obtained from Aldrich. PEGMA-*b*-PAEMA polymers were synthesized by reversible addition-fragmentation chain transfer (RAFT) controlled radical polymerization.[24] Their molecular characterization was carried out by ^1H NMR spectroscopy and size exclusion chromatography (SEC). The results are shown in Table S1 (Supporting Information).

CICHA were prepared by employing the gas diffusion method at room temperature. The use of this method allows for a slow progression of the precipitation reaction. In a typical run, an aqueous solution containing 1 g L^{-1} of PEGMA-*b*-PAEMA and 40×10^{-3} M of $Cu(CH_3COO)_2$ was prepared using double-distilled (DI) water that had been purged with nitrogen overnight. First, a 25 mL glass vial was placed that was loaded with ammonium carbonate powder and covered with parafilm at the bottom of a desiccator. Then 20 mL of the prepared solution was injected into a 50 mL beaker, covered the vial with parafilm, and placed the beaker into the same desiccator. Before closing the desiccator, three needle holes were punched in each parafilm. Blue-gray colored precipitates were gradually deposited from the colloidal solution of PEGMA-*b*-PAEMA and $Cu(CH_3COO)_2$ with the diffusion of CO_2 and

NH_3. After 3 days, the precipitate was collected and isolated by ultracentrifugation. Ultracentrifugation separation was run at 20 °C under 35 000 rpm for three times, each time for 30 min. Each time before ultracentrifugation, the sample was dispersed via ultrasonication. For the first cycle, DI H_2O was used as solvent. For the next two cycles, ethanol instead of DI H_2O was used as solvent. Finally, samples were dried under a vacuum at ambient temperature. The final products were obtained as green-gray powders.

Characterization: ^1H NMR spectra were recorded in $CDCl_3$ with tetramethylsilane (TMS) used as an internal standard on an Avance Bruker 300 MHz spectrometer.

The average molecular weights (MWs) and polydispersity indices (PDI) of the block copolymers were determined by SEC using equipment supplied by Polymer Standards Service (PSS). All measurements were carried out at room temperature. The mobile phase was THF, delivered at a flow rate of 1 mL min^{-1}. The refractive index was measured with a Waters 2414 refractive index detector. The instrumentation was calibrated using poly(methyl methacrylate) (PMMA) standards supplied by PSS.

DLS measurements performed at a 90° scattering angle were carried out using a 90Plus Brookhaven DLS spectrometer equipped with a 30 mW laser operating at 633 nm. Solution concentrations were maintained at 4 g L^{-1}. Prior to DLS measurements, all polymer solutions were filtered through cellulose acetate microfilters (pore size: 0.45 µm).

SEM measurements were performed on a LEO 1550 – GEMINI microscope. Powder XRD patterns were recorded on a PDS 120 diffractometer (Nonius GmbH, Solingen) with CuKα radiation ($\lambda = 1.542$ Å). Thermogravimetric analysis was carried out under a stream of nitrogen, at a heating rate of 10 °C min^{-1} using a Netzsch TGA-209. TEM and SAED were obtained on a JEOL-2010 microscope operated at 200 kV. The samples were embedded in epoxy resin and ultramicrotomed for the TEM measurements. The AFM analysis was performed on a Digital Instruments nanoscope IIIa Multimode AFM. Solution samples of PEGMA-*b*-PAEMA were prepared for AFM measurements by dissolving the polymer substances in aqueous solutions, dispersing the solution sample on pre-cleaned silicon wafer by spin-coating at 3500 rpm for 1 min, and setting it aside to dry. After the sample was dried, AFM imaging was conducted. The magnetic susceptibility measurements were carried out using a Quantum Design MPMS XL-7 SQUID magnetometer operating in the temperature range of 2–300 K and in a field up to 5 T.

Supporting Information

Supporting Information is available from the Wiley Online Library or from the author.

Acknowledgements

The authors gratefully acknowledge Anne Heilig for her help in AFM measurements, Xiaolan Yu (Sun Yat-Sen University, China) for his help in magnetization measurements, and Dr. Petri Papaphilippou (University of Cyprus) for the synthesis of the PEGMA-b-PAEMA additives. Prof. Pierre Rabu (IPCMS, France) is acknowledged for providing the CIF file of CHA. This work was financially supported by the Max-Planck-Society. The manuscript was written through contributions of all authors. All authors have given approval to the final version of the manuscript. The authors declare no competing financial interests.

[1] P. Rabu, M. Drillon, K. Awaga, W. Fujita, T. Sekine, (Eds: J. S. Miller, M. Drillon, *Magnetism: Molecules to Materials IV.*), Wiley-VCH, Weinheim, Germany **2002**, pp. 357–395.
[2] K. Suzuki, J. Haines, P. Rabu, K. Inoue, M. Drillon, *J. Phys. Chem. C* **2008**, *112*, 19147.
[3] A. Jiménez-López, E. Rodriguez-Castellón, P. Olivera-Pastor, P. Maireles-Torres, A. A. G. Tomlinson, D. J. Jones, J. Rozière, *J. Mater. Chem.* **1993**, *3*, 303.
[4] N. Masciocchi, E. Corradi, A. Sironi, G. Moretti, G. Minelli, P. Porta, *J. Solid State Chem.* **1997**, *131*, 252.
[5] F. Yang, C. Massobrio, M. Boero, *J. Phys. Chem. C* **2014**, *118*, 18700.
[6] F. Yang, M. Boero, C. Massobrio, *J. Phys. Chem. C* **2010**, *114*, 20213.
[7] G. Rogez, C. Massobrio, P. Rabu, M. Drillon, *Chem. Soc. Rev.* **2011**, *40*, 1031.
[8] S. Yamanaka, T. Sako, M. Hattori, *Chem. Lett.* **1989**, *10*, 1869.
[9] S. H. Park, C. H. Lee, C. E. Lee, H. C. Ri, S. Y. Shim, *Mater. Res. Bull.* **2002**, *37*, 1773.
[10] V. Laget, C. Hornick, P. Rabu, M. Drillon, *J. Mater. Chem.* **1999**, *9*, 169.
[11] W. Fujita, K. Awaga, *Inorg. Chem.* **1996**, *35*, 1915.
[12] W. Fujita, K. Awaga, T. Yokoyama, *Appl. Clay Sci.* **1999**, *15*, 281.
[13] W. Fujita, K. Awaga, T. Yokoyama, *Inorg. Chem.* **1997**, *36*, 196.
[14] G. W. Pratt, *Phys. Rev.* **1957**, *108*, 1233.
[15] J. Brabers, K. H. J. Buschow, F. R. de Boer, *Phys. Rev. B* **1999**, *59*, 9314.
[16] R. Q. Song, H. Colfen, *CrystEngComm* **2011**, *13*, 1249.
[17] O. Klimm, C. Gobel, S. Rosenfeldt, F. Puchtler, N. Miyajima, K. Marquardt, M. Drechsler, J. Breu, S. Forster, B. Weber, *Nanoscale* **2016**, *8*, 19058.
[18] S. Acharya, S. Sutradhar, J. Mandal, K. Mukhopadhyay, A. K. Deb, P. K. Chakrabarti, *J. Magn. Magn. Mater.* **2012**, *324*, 4209.
[19] C. Mix, G. Jakob, *J. Appl. Phys.* **2013**, *113*, 17D907.
[20] C. Abad-Zapatero, *Nature* **1992**, *356*, 392.
[21] J. E. Pitts, *Nature* **1992**, *355*, 117.
[22] C. Lausser, H. Colfen, M. Antonietti, *ACS Nano* **2011**, *5*, 107.
[23] M. Chen, H. Colfen, S. Polarz, *Z. Naturforsch., B: J. Chem. Sci.* **2013**, *68*, 103.
[24] P. Papaphilippou, L. Loizou, N. C. Popa, A. Han, L. Vekas, A. Odysseos, T. Krasia-Christoforou, *Biomacromolecules* **2009**, *10*, 2662.
[25] T. Krasia, H. Schlaad, in *Metal-Containing and Metallosupramolecular Polymers and Materials* (Eds: U. S. Schubert, G. R. Newkome, I. Manners), American Chemical Society, Washington DC, USA **2006**, pp. 157–167.
[26] C. J. Stephens, S. F. Ladden, F. C. Meldrum, H. K. Christenson, *Adv. Funct. Mater.* **2010**, *20*, 2108.
[27] R. Erhardt, A. Boker, H. Zettl, H. Kaya, W. Pyckhout-Hintzen, G. Krausch, V. Abetz, A. H. E. Mueller, *Macromolecules* **2001**, *34*, 1069.
[28] S. C. Warren, F. J. Disalvo, U. Wiesner, *Nat. Mater.* **2007**, *6*, 248.
[29] D. Jones, *Nature* **1992**, *358*, 546.
[30] R. W. G. Wyckoff, R. B. Corey, *Science* **1936**, *84*, 513.
[31] D. P. Kozlenko, A. V. Rutkauskas, N. T. Dang, N. O. Golosova, S. E. Kichanov, L. S. Dubrovinsky, H. P. Liermann, W. Morgenroth, B. N. Savenko, *JETP Lett.* **2014**, *100*, 380.

[32] O. Isnard, V. Paul-Boncour, Z. Arnold, C. V. Colin, T. Leblond, J. Kamarad, H. Sugiura, *Phys. Rev. B* **2011**, *84*, 094429.
[33] A. D. Molina-Garcia, *Prog. Colloid Polym. Sci.* **1999**, *113*, 57.
[34] W. F. Harrington, G. Kegeles, *Methods Enzymol.* **1973**, *27*, 306.
[35] R. Q. Song, A. W. Xu, S. H. Yu, *J. Am. Chem. Soc.* **2007**, *129*, 4152.
[36] R. Q. Song, A. W. Xu, B. Deng, Q. Li, G. Y. Chen, *Adv. Func. Mater.* **2007**, *17*, 296.
[37] C. Frandsen, S. Mørup, *J. Phys. Condens. Matter* **2006**, *18*, 7079.
[38] H. Cölfen, M. Antonietti, *Mesocrystals and Nonclassical Crystallization*, Wiley, Chichester, UK **2008**.
[39] G. N. Rao, Y. D. Yao, J. W. Chen, in *INTERMAG Asia 2005, Digests of the IEEE Int. Magnetics Conf.*, Institute of Electrical and Electronics Engineers, Scataway, N.J., USA, **2005**, p. 1049.
[40] T. G. Sorop, M. Evangelisti, M. Haase, L. J. de Jongh, *J. Magn. Magn. Mater.* **2004**, *272*, 1573.
[41] S. H. Kilcoyne, R. Cywinski, *J. Magn. Magn. Mater.* **1995**, *140*, 1466.
[42] W. J. Schuele, V. D. Deetscreek, *J. Appl. Phys.* **1962**, *33*, 1136.
[43] C. Frandsen, C. R. H. Bahl, B. Lebech, K. Lefmann, L. T. Kuhn, L. Keller, N. H. Andersen, M. von Zimmermann, E. Johnson, S. N. Klausen, S. Mørup, *Phys. Rev. B* **2005**, *72*, 214406.
[44] J. U. Thiele, M. Buess, C. H. Back, *Appl. Phys. Lett.* **2004**, *85*, 2857.
[45] J. W. Kim, P. J. Ryan, Y. Ding, L. H. Lewis, M. Ali, C. J. Kinane, B. J. Hickey, C. H. Marrows, D. A. Arena, *Appl. Phys. Lett.* **2009**, *95*, 222515.
[46] S. S. Rao, S. Tripathi, D. Pandey, S. V. Bhat, *Phys. Rev. B* **2006**, *74*, 144416.
[47] Y. J. Tang, D. J. Smith, B. L. Zink, F. Hellman, A. E. Berkowitz, *Phys. Rev. B* **2003**, *67*, 054408.
[48] V. H. Crawford, H. W. Richardson, J. R. Wasson, D. J. Hodgson, W. E. Hatfield, *Inorg. Chem.* **1976**, *15*, 2107.
[49] E. Ruiz, M. Llunell, J. Cano, P. Rabu, M. Drillon, C. Massobrio, *J. Phys. Chem. B* **2006**, *110*, 115.
[50] E. Ruiz, P. Alemany, S. Alvarez, J. Cano, *J. Am. Chem. Soc.* **1997**, *119*, 1297.
[51] M. Manekar, S. B. Roy, *J. Phys. Condens. Matter* **2008**, *20*, 325208.